3-D Inversion of Helicopter EM Data

Börner, R.-U.[1], Afanasjew, M.[2], Eiermann, M.[2], Ernst, O. G.[2], Scheunert, M.[1], Spitzer, K.[1]

[1]Institute of Geophysics and Geoinformatics, [2]Institute of Numerical Analysis and Optimization

Introduction

Airborne electromagnetic methods quickly provide resistivity maps of large areas. These resistivities are obtained from layered half-space models. However, the underlying 1-D assumption is often violated. In such cases, a full 3-D inversion has to be carried out. By defining appropriate dimensionality indicators (Fig. 1) it is possible to reduce the amount of data to be inverted. In this poster, we demonstrate a 3-D inversion approach for multi-frequency helicopter electromagnetic data. For preliminary studies, we invert a synthetic data set for a simple model problem as published by Siemon et al. (2009). The research is carried out in an interdisciplinary project called 'AIDA' which was funded by the German Ministry of Education and Research BMBF and the German Research Foundation DFG under the Geotechnologien Programme, grant 03G0735D.

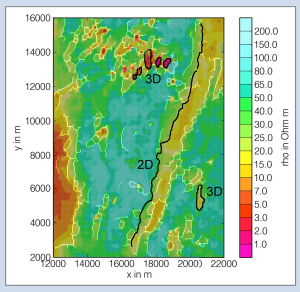

Figure 1: Typical resistivity map derived from an airborne survey. Due to large lateral gradients in the resistivity distribution, areas indicated by "2-D" and "3-D" can not be interpreted with 1-D models.

The forward problem

Maxwell's curl-curl equations in their quasi-static approximation for the secondary electric field can be expressed within a bounded domain $\Omega \subset \mathbb{R}^3$ as

$$\nabla \times \nabla \times \boldsymbol{E}_s + i\omega\mu\sigma \boldsymbol{E}_s = -i\omega\mu \boldsymbol{j}_p \text{ in } \Omega \tag{1}$$

$$\boldsymbol{n} \times \boldsymbol{E}_s = 0 \qquad \text{at } \partial\Omega, \tag{2}$$

where $\boldsymbol{j}_p(\boldsymbol{r}) = (\sigma(\boldsymbol{r}) - \sigma_0(z))\boldsymbol{E}_p(\boldsymbol{r})$ acts as a source current density driven by the primary electric field of a dipole source located above a stratified earth with electrical conductivity $\sigma_0(z)$.
After spatial discretization on a finite difference (FD) or finite element (FE) grid, the continuous boundary value problem has been transformed into a system of linear equation as

$$\boldsymbol{A}(\sigma)\boldsymbol{u}_s = \boldsymbol{b}, \tag{3}$$

where $\boldsymbol{A}(\sigma) = \boldsymbol{K} + i\omega\boldsymbol{M}(\sigma)$ is a sparse, complex-valued, symmetric, and typically large matrix. The right-hand side $\boldsymbol{b}$ contains the discretized source terms. The solution of the linear system yields the discrete secondary electric field $\boldsymbol{u}_s$. Generally, the location of the spatial locations where the field components are sampled may differ from the location of the discrete field components within the computational domain. Therefore, *mapping* or *measurement operators* $\boldsymbol{Q}$ have to be defined yielding the total fields

$$\boldsymbol{E}(\boldsymbol{r}) = \boldsymbol{Q}^E(\boldsymbol{r})[\boldsymbol{u}_s] + \boldsymbol{E}_p(\boldsymbol{r}) \tag{4}$$

$$\boldsymbol{H}(\boldsymbol{r}) = \boldsymbol{Q}^H(\boldsymbol{r})\boldsymbol{C}^E[\boldsymbol{u}_s] + \boldsymbol{H}_p(\boldsymbol{r}). \tag{5}$$

The operators $\boldsymbol{Q}^E$ and $\boldsymbol{Q}^H$ provide the sought quantities by forming a linear combination of the relevant components of the discrete solution vector.

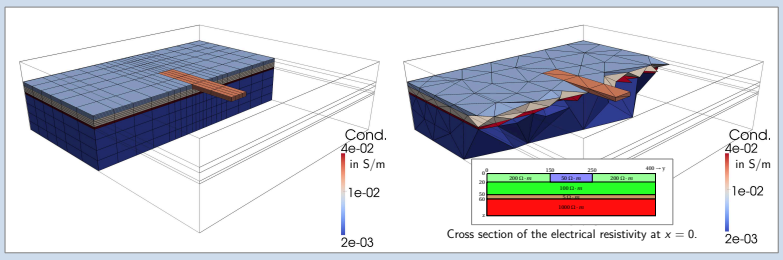

Figure 2: Discretization of an electrical conductivity distribution on a finite difference grid (left) and finite element grid (right). Flight profiles for gathering of the synthetic data are laid out perpendicular to the strike of the conductive body (faded red, completely shown) at a height of $h = 30$ m above ground.

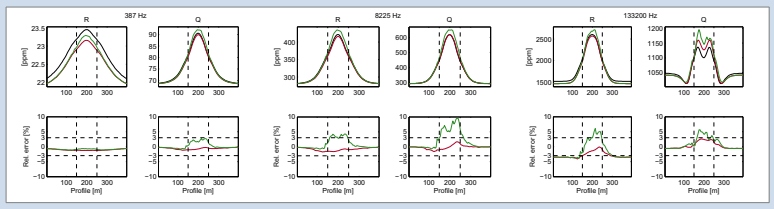

Figure 3: Comparison of solution obtained by an FD discretization (red) and an FE discretization (green) with a reference solution obtained by an integral equation (IE) code by Avdeev et al. (1998). The top panel indicates real (R) and imaginary (Q) parts of the normalized magnetic field at the receiver for three distinct frequencies. Data has been simulated along a profile perpendicular to the conductive body (Fig. 2). The lower panel indicates the relative error with respect to the IE solution.

Generation of synthetic data

For the numerical experiments we have computed synthetic data for the three profiles Line 2.1, 3.1, and 4.1 shown in Fig. 4. The lateral distance of the flight profiles is 200 m. Along the profiles a spacing of 4 m has been chosen. The length of the flight paths is 1000 m. Data has been collected for five distinct frequencies. In total, we have generated 3765 complex-valued data points.

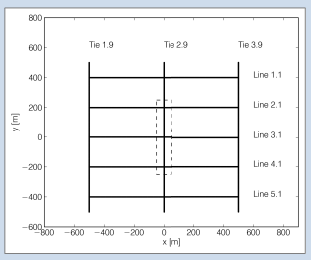

Figure 4: Flight profiles for computation of synthetic data.

The inverse problem

We aim at finding a model parameter distribution, i. e., $\boldsymbol{m} = \log\boldsymbol{\sigma}$, $\boldsymbol{m} \in \mathbb{R}^M$, such that both the difference between measured data $\boldsymbol{d}^{\text{obs}}$ and predicted data from the forward solution for a given model parameter set as well as the parameter roughness are minimal:

$$\frac{1}{2}\left\|\boldsymbol{d}^{\text{obs}} - \boldsymbol{Q}\boldsymbol{A}^{-1}(\boldsymbol{m})\,\boldsymbol{b}\right\|_2^2 + \frac{\lambda}{2}\left\|\boldsymbol{W}[\boldsymbol{m} - \boldsymbol{m}_{\text{ref}}]\right\|_2^2 \to \text{min!} \tag{6}$$

A linearization of the forward operator with respect to the model parameters is required for the solution of the inverse problem. The sensitivity equation approach yields expressions for the partial derivative of the predicted data with respect to the model parameters

$$\boldsymbol{J} := \frac{\partial \boldsymbol{d}}{\partial \boldsymbol{m}} = \boldsymbol{Q}\boldsymbol{A}^{-1}\boldsymbol{L} \tag{7}$$

with

$$\boldsymbol{L} = \frac{\partial \boldsymbol{b}}{\partial \boldsymbol{m}} - \frac{\partial \boldsymbol{A}}{\partial \boldsymbol{m}} \times_2 \boldsymbol{u}. \tag{8}$$

The Gauss-Newton method yields a model update. Based on the resulting system of normal equations

$$[\boldsymbol{J}^H\boldsymbol{J} + \lambda\boldsymbol{W}^T\boldsymbol{W}]\Delta\boldsymbol{m} = \boldsymbol{J}^H[\boldsymbol{d}^{\text{obs}} - \boldsymbol{Q}\boldsymbol{A}^{-1}(\boldsymbol{m})\,\boldsymbol{b}] - \lambda\boldsymbol{W}^T\boldsymbol{W}[\boldsymbol{m}_0 - \boldsymbol{m}_{\text{ref}}] \tag{9}$$

with

$$\boldsymbol{m} = \boldsymbol{m}_0 + \Delta\boldsymbol{m} \tag{10}$$

the least squares problem can be solved for the model update $\Delta\boldsymbol{m}$ by Krylov subspace methods, such as CG or LSQR. Note that Krylov methods avoid the explicit forming of the Jacobian $\boldsymbol{J}$. Instead, only the action of the Jacobian on a vector is necessary, which requires the solution of a forward problem at each Krylov iteration. A factorization of the system matrix $\boldsymbol{A}$ can substantially reduce the numerical effort required for the solution of systems with multiple right-hand sides.

Line search

The curves in Fig. 5 result from the underlying linearized (black) and the nonlinear (blue) minimization problem as well as from an approximation to the corresponding objective function of the latter (red). Concerning a fixed model update, we aim at finding the minimum of the blue curve (blue star), but we actually calculate the function value that results from the minimum of the Gauss-Newton method (right triangle and black star, respectively). To overcome this discrepancy, we apply a line search algorithm which gives an approximate step length derived from the minimum of a quadratic function (red star).

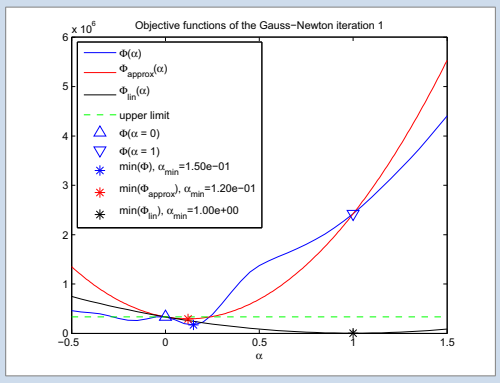

Figure 5: Objective functions of the least squares problem with respect to the step length α.

Inversion results

M	DOF	Iter_{GN}	$\varnothing\text{Time}_{\text{fwd}}$	$\varnothing\text{Time}_{\text{GN}}$	Time_{tot}
144	2952	14	5.4 s	51.3 s	771 s
1152	43127	12	180.7 s	1280.2 s	≈ 4 h
1152	102258	14	615.6 s	3799.4 s	≈ 19 h

Timings for different complexities of the parameter mesh and adaptively refined meshes for the forward problem. The maximum number of the inner CG iterations is limited to 50 in each case.

Fig. 6 shows the inverted parameter cells which are located in a restricted inversion area. This inner area is adapted from the sensitivity distribution of the homogeneous case and includes a subset of nearly all domains of the original modeling area. We therefore used a homogeneous starting model and an exponentially decreasing regularization parameter.

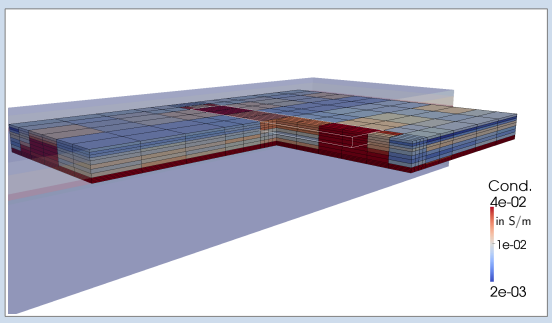

Figure 6: Inversion result for the 1152 model parameters.

Outlook

Further studies will incorporate more involved weighting strategies for unstructured grids as well as the exploration of automatic updating schemes for the regularization parameter. Additionally, we aim at the investigation of case studies for real helicopter measurement data sets.

Avdeev, D., Kuvshinov, A., Pankratov, O., and Newman, G. (1998). *Three-dimensional frequency-domain modeling of airborne electromagnetic responses.* Exploration Geophysics, 29(2):111–119.

Siemon, B., Auken, E., and Christiansen, A. (2009). *Laterally constrained inversion of helicopter-borne frequency-domain electromagnetic data.* Journal of Applied Geophysics, 67:259–268.

Contact:
Ralph-Uwe Börner
rub@geophysik.tu-freiberg.de

Funded by
Bundesministerium für Bildung und Forschung